Intraoperative Laparoscope Augmentation for Port Placement and Resection Planning in Minimally Invasive Liver Resection

Marco Feuerstein*, Thomas Mussack, Sandro M. Heining, and Nassir Navab

Abstract—In recent years, an increasing number of liver tumor indications were treated by minimally invasive laparoscopic resection. Besides the restricted view, two major intraoperative issues in laparoscopic liver resection are the optimal planning of ports as well as the enhanced visualization of (hidden) vessels, which supply the tumorous liver segment and thus need to be divided (e.g., clipped) prior to the resection. We propose an intuitive and precise method to plan the placement of ports. Preoperatively, self-adhesive fiducials are affixed to the patient's skin and a computed tomography (CT) data set is acquired while contrasting the liver vessels. Immediately prior to the intervention, the laparoscope is moved around these fiducials, which are automatically reconstructed to register the patient to its preoperative imaging data set. This enables the simulation of a camera flight through the patient's interior along the laparoscope's or instruments' axes to easily validate potential ports. Intraoperatively, surgeons need to update their surgical planning based on actual patient data after organ deformations mainly caused by application of carbon dioxide pneumoperitoneum. Therefore, preoperative imaging data can hardly be used. Instead, we propose to use an optically tracked mobile C-arm providing cone-beam CT imaging capability intraoperatively. After patient positioning, port placement, and carbon dioxide insufflation, the liver vessels are contrasted and a 3-D volume is reconstructed during patient exhalation. Without any further need for patient registration, the reconstructed volume can be directly augmented on the live laparoscope video, since prior calibration enables both the volume and the laparoscope to be positioned and oriented in the tracking coordinate frame. The augmentation provides the surgeon with advanced visual aid for the localization of veins, arteries, and bile ducts to be divided or sealed.

Index Terms—Augmented reality visualization, image-guided surgery, laparoscopic surgery, port placement.

I. INTRODUCTION

THE liver is one of the most frequently targeted organs for primary and secondary malignant lesions. Hepatocellular carcinoma (HCC) and metastasis of colorectal neoplasms are the most common diagnoses. HCC with about one million newly registered cases worldwide each year is the fourth most frequent cancer related cause of death. Without medical treatment, HCC will lead to death in 100% of the cases. At present, only about 5%–15% of diagnosed cases can be treated by the surgical resection of malignant regions, which is standard of care. Ablation and chemotherapy do not provide a sufficient success rate. The average five year survival rate only lies between 30% and 40% [1].

Since 1991, laparoscopic liver resection is performed for an increasing number of cases, as it is less invasive than laparotomy (open surgery) and, hence, less harmful to the patient. Unfortunately, laparoscopic surgery itself introduces several drawbacks at the same time. The localization of the target region, i.e., the vessels to be sealed or divided, is difficult to achieve due to a restricted working space and a visualization solely limited to the view of the laparoscope onto the liver surface. Additionally, up to 14% of laparoscopic interventions need to be converted to open laparotomy because of intraoperative bleeding [2]. Here, a selective minimally invasive therapy enabled by enhanced intraoperative imaging will be of great benefit.

A. Port Placement

Ideal port placement, i.e., finding the optimal trocar incision sites for all instruments, is one of the key issues in minimally invasive laparoscopic surgery. The optimal choice of the instruments' ports provides full access to the whole operation region as well as adequate surgeon dexterity. This can avoid time-consuming new port placement which may cause considerable pain and extended recovery for every patient. Even experienced surgeons sometimes require port replacements during difficult interventions such as vessel dissection and lymph node dissection of the hepatoduodenal ligament or along the vena cava inferior, so an exact port placement is of great importance.

In the current clinical workflow, the surgical staff selects all ports by palpation of external anatomic landmarks, primarily based on their previous experience. However, if these external landmarks do not correspond to the individual internal anatomy of each patient, a misplacement of ports can occur. Several methods have been proposed to improve and automate the

optimal placement of ports [3]–[7]. They manually or semi-automatically segment preoperative imaging data from computed tomography (CT) or magnetic resonance (MR) imaging, which is essential to reconstruct models of the anatomy, e.g., ribs, liver, and soft tissue. These 3-D models can be used to manually plan ports in an interactive virtual environment [3], [4] or automatically compute optimal port locations [5]–[7], which serve as important guidelines for surgeons. This can greatly improve the learning curve especially of untrained surgeons. Finally, a practical and accurate way of transfering the planned port locations to the operating room is needed, meaning the patient has to be registered to his/her preoperative data.

This patient registration process is usually based on matching anatomical or artificial landmarks, which are visible on both the patient and its preoperative data. Adhami and Coste-Manière use the end effectors of the da Vinci surgical system to point to fiducials, which are attached to the patient [8]. Due to their shape and intensity, the fiducials can be segmented automatically in the CT data. Intraoperatively, the (sterile) surgical staff moves a robot arm's end effector to every single fiducial in order to get its position in the robot coordinate frame. As reported by Falk et al. [9], this task takes approximately 2 min. Similarly, Selha et al. use the sensor of an additional electromagnetic tracking system as a pointing device, basing their registration on anatomical landmarks [10]. For a laser projection of optimal ports, Marmurek et al. utilize an optically tracked pointer to perform registration on the basis of physical landmarks [7]. Coste-Manière et al. also compared their fiducial based registration method to a surface based approach, which uses a camera and a projector to facilitate patient reconstruction from structured-light images [11].

We propose a practical alternative method to register the CT data to the patient. After successful application of this method to phantom data [12], here we present our first results of in vivo experiments. Spherical CT visible self-adhesive fiducials are affixed on the patient's skin. They are segmented automatically in the patient's CT data. Intraoperatively, instead of pointing to the fiducials, we only move the tracked laparoscope around the fiducials and acquire a set of images from differing, but arbitrary poses. The fiducials are automatically detected in these images. To simplify the detection process, the laparoscope is pivoted around each fiducial, so sufficiently sized images of the fiducial can be obtained for an accurate determination of its 2-D image coordinates. From at least two images, the 3-D position of each fiducial is reconstructed in the tracking (=world) coordinate frame. Point based graph matching and registration methods enable us to match the fiducials with their counterparts in the CT data.

For port placement, a surgical staff member simply moves the tracked instruments or laparoscope to the positions where he/she wishes to place their corresponding ports. A virtual camera is placed on top of the instruments' end effectors or the laparoscope's camera center. It is able to simulate a flight through the patient's interior by rendering the CT volume as it would be seen by the laparoscope. In this natural way, optimal port placements can easily be identified without prior segmentation of patient's anatomy or the use of a pointing device. In addition, there is no need to identify anatomical landmarks or touch artificial landmarks, which for da Vinci usually has to be performed by the physician controlling the system or by other surgical staff such as (trained) scrub nurses. Our method is applicable to any tracked laparoscope, no matter whether it is tracked by an optical tracking system or a mechanical one such as da Vinci, and can also be performed by any surgical staff member.

B. Intraoperative Vessel Visualization

Mala et al. [2] provide a good insight into a typical totally laparoscopic liver resection procedure. First, three to five trocars sized 11 and 12 mm are used to insert the instruments and a 30° laparoscope. Pneumoperitoneum is applied, i.e., carbon dioxide (CO_2) is insufflated into the abdomen to provide better visualization and exposure. Electrocauterization is utilized to mark the area to be resected on the liver surface. At the beginning of the resection, outer small vessels and bile ducts are sealed by an ultrasonic scalpel. An ultrasound (US) surgical aspirator can be used to fracture and evacuate liver tissue deeper inside the liver. An ultrasonic scalpel, diathermy, or clips can be applied to divide minor vessels and bile ducts, which remain preserved, while larger ones can be divided by a stapling device or clips. To guide the division of vessels and eventually the resection, ultrasonography may be used.

For orthopedics and neurosurgery, where mainly rigid structures are involved, navigation systems aligning preoperative imaging data in respect to the patient are commercially available.[1]

For laparoscopic abdominal surgery, the target region can be deformed due to the heartbeat and respiratory motion. As shown by Olbrich et al. [13], deformations in the abdominal area caused by the heartbeat are negligible. The rather large respiratory motion of about 1 cm [14], [15] can be corrected for by gating [16]. As expiration and inspiration plateaus are reproducible within about 1 mm under active breathing control [17], but also under normal breathing [15], they can be synchronized to e.g., an augmented visualization [13]. Nicolau et al. are currently investigating on respiratory motion correction, considering either gating or deformable registration [18]. Up to now, they use rigidly registered preoperative CT data and a tracked needle for the guidance of radio-frequency tumor ablation, where no pneumoperitoneum is applied. Their achieved average accuracy for tumor localization was 9.5 mm. They also presented initial experiments on a rigid abdominal phantom, where they applied their system to laparoscopic surgery [19].

Individual deformations of greater extent mainly occur between preoperative acquisition of the CT and the beginning of the resection, i.e., during patient and port placement, appliance of CO_2 pneumoperitoneum, and the intervention itself. Pneumoperitoneum alone can already cause large liver motions of e.g., 1.8 ± 12, 4.1 ± 6.4, and 0.1 ± 0.4 mm in x, y, and z directions, respectively, as shown for two pigs by Herline et al. [14]. In this case, using preoperative rigid imaging data to support the surgeon in updating the surgical resection planning is difficult to perform and hard to validate. For robot assisted coronary artery bypass, Mourgues et al. therefore proposed an

---

[1]For example, by Aesculap, BrainLAB, Medtronic, ORTHOsoft, PI Systems, Praxim Medivision, and Stryker

intelligent way to intraoperatively update the model of a preoperative coronary tree [20]. Interactively, the surgeon identifies and marks visual clues in the endoscope images, so an algorithm can estimate a better intraoperative registration of the coronary tree model. *In vivo* experiments showed an accuracy of about 9.3–19.2 mm [9].

Furthermore, several attempts were made to use intraoperative imaging. In general, MR scanners are too bulky to be used during laparoscopic surgery or require the patient to be moved for the acquisition, making a precise intraoperative registration almost impossible. Fichtinger *et al.* developed an inventive intraoperative CT image overlay system based on a semitransparent mirror for the purpose of needle insertion, where no major deformations are involved [21]. Keeping it simple and inexpensive, only a single 2-D CT slice is shown, which is sufficient for "in-plane" procedures such as needle placement. It is difficult to apply their system to laparoscopic vessel augmentation, where volumetric 3-D data is essential.

In case of intraoperative guidance by ultrasonography, it is difficult to understand, how US images are oriented in relation to the patient. Ellsmere *et al.* therefore propose an advanced system to intuitively display the laparoscopic US image plane relative to a preoperative 3-D model of the patient [22], [23]. This helps the physician to identify anatomical key structures and to learn the use of laparoscopic ultrasound. An ideal complement to their navigation system would be the provision of registered intraoperative 3-D data of high quality, which is not affected by the individual organ movement between preoperative data acquisition and the beginning of the intervention (after CO_2 insufflation) and could be used instead of the preoperative CT to accomplish the guidance.

Another approach to improve the spatial relation of US images to the patient is taken by Leven *et al.* [24]. They propose a system to apprehensively overlay the laparoscopic ultrasound image plane or a reconstructed US volume, respectively, directly on the live images of a stereo endoscope. It is however still difficult to interpret low-resolution US images, especially reconstructed volumes. Providing a high-resolution 3-D volume intraoperatively and combining it with advanced visualization could be an optimal supplement to their system as well.

To provide registered high-resolution 3-D data supplementary to laparoscopic ultrasound, we use a mobile isocentric C-arm providing cone-beam CT imaging capability [25] to visualize soft tissue intraoperatively, which is hardly possible with current commercially available mobile C-arms. An optical tracking system determines the position and orientation of both C-arm and laparoscope, which can be brought into the same tracking coordinate system by various calibration routines, as described in Section II-B. This makes the intraoperative soft tissue visualization of our system registration-free, i.e., *patient or patient imaging data is not used for registration*, but is intrinsically registered to the tracking system. Therefore, there is no need for detection and matching of anatomical landmarks or fiducials on the patient, as used during port placement (cf. previous Section I-A). Registration-free systems are solely based on reconstruction, navigation, and visualization, all in an external tracking coordinate system. In their review on image-guided procedures Yaniv and Cleary note several registration-free systems [26]. At our Chirurgische Klinik we use a registration-free system routinely on a daily basis for spine, pelvis, hip, knee, and ankle surgery.[2] In this paper, we introduce the use of an optical imaging system, i.e., laparoscope, within a registration-free navigation system. This is the first time two different imaging systems are integrated using the registration-free concept. After a promising *ex vivo* evaluation of the registration-free concept [27], we here present our first *in vivo* results.

Intraoperatively, after port and trocar[3] placement and application of CO_2 pneumoperitoneum, we contrast the vessel tree of the liver and at the same time acquire an image series during patient exhalation. Alternatively, C-arm projections can be gated and correlated to respiratory motion in order to acquire a high-quality scan, as Kriminski *et al.* suggested [28]. After reconstruction, we are able to precisely augment the contrasted vessel tree directly on the laparoscopic view just before the beginning of the resection without any time-consuming patient registration process. The augmentation can be synchronized to the patient's respiration and only be displayed during exhalation [13]. This provides the surgeon with valuable information on the location of veins, arteries, and bile ducts, which supply the liver segment to be resected and which therefore need to be divided. In general, the augmented visualization will only be shown to the surgeon for the intraoperative *in situ* planning of the resection to provide a detailed "road map" of the vessels, but not any more when the surgeon starts to cut, since this causes the liver to deform again and invalidates any prior intrinsic registration. Only if crucial problems appear, another image series may be acquired and an intrinsically registered volume reconstructed.

To take full advantage of the 3-D data, which gets partially lost during the 2-D projection on the laparoscope video, the surgical staff can also analyze the data on a separate monitor by moving through or around the 3-D cone-beam CT reconstruction. Alternatively, a laparoscopic virtual mirror can be utilized, which visualizes a reflected side view of the liver and its vessels [29]. By interactively moving the virtual mirror within the augmented monocular view of the laparoscope, the surgical staff is able to observe the 3-D structure of the blood vessels.

One may argue to also use cone-beam C-arm data (instead of preoperative CT data) for port placement planning. Unfortunately, this can hardly be justified due to following reasons: 1) The size of a reconstructed C-arm volume is $20 \times 20 \times 15\,\mathrm{cm}^3$, which only partially covers the patient anatomy needed for port placement planning. 2) Patients usually get one or more preoperative diagnostic CT scans. If fiducials are already attached to a patient for these scans, their data can be used for port placement planning. 3) The same data set used for liver resection planning cannot be used for port placement planning due to organ move-

---

[2]In detail, we use the SurgiGATE system by Medivision for: spine (pedicle screw placement, decompression of the spinal canal, control of achieved reposition, spinal tumor resection); pelvis (minimally invasive percutaneous placement of SI-screws (sacro-iliacal screws), minimally invasive acetabular reconstruction); hip: (screw osteosynthesis of femoral neck fractures); knee (minimally invasive reconstruction of tibia plateau fractures, screw placement and control of reduction); ankle [retrograde drilling (core decompression) in osteochondrosis dissecans tali(OD $2°$–$3°$)].

[3]All trocars are made of plastic, so they do not give artifacts in the cone beam reconstruction.
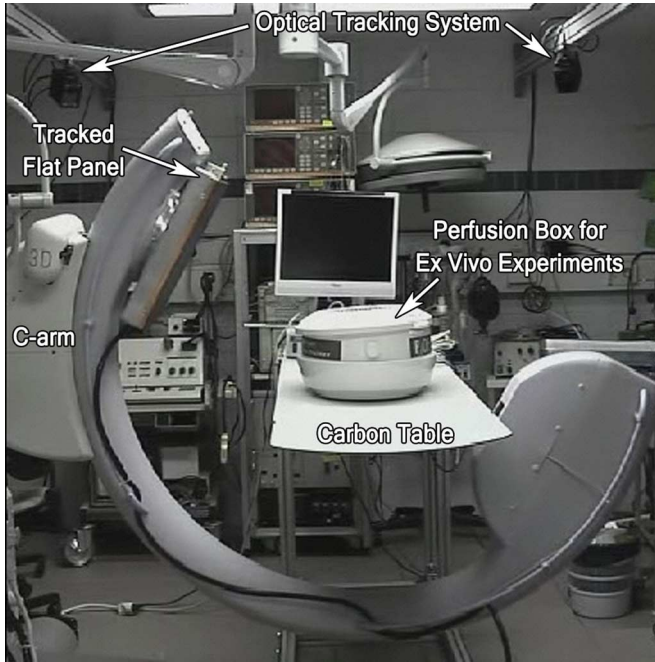
Fig. 1. Arrangement of our experimental setup in the animal operating room.

Fig. 2. All coordinate frames, which need to be brought into a common world coordinate system.

ments caused by CO_2 insufflation. Radiation and contrast agent exposure caused by an additional scan only for port placement can hardly be justified.

II. SYSTEM OVERVIEW

In order to augment the laparoscope with preoperative CT data and intraoperative C-arm data, an elaborate system was set up in our experimental animal operating room, as visualized on Fig. 1.

A. System Setup

The prototype mobile C-arm is based on a Siemens Power-Mobil and incorporates a workstation deployed with acquisition and reconstruction software by Siemens. We attached four retroreflective spherical markers (also referred to as marker targets) to the flat-panel detector of the C-arm [cf. Fig. 4(a)]. These markers are seen by four optical tracking cameras (ARTtrack2, ART GmbH, Weilheim, Germany) mounted just beneath the operating room's ceiling, one in each corner of a rectangle. The tracking system is connected to a PC equipped with a tracking software that is able to send 6-D tracking data over Ethernet to our navigation workstation. This navigation workstation is also connected to the C-arm workstation via Ethernet to directly access any reconstructed volumes. A frame grabber is incorporated that captures the live video of our laparoscope with 30° optics (KARL STORZ GmbH and Company KG, Tuttlingen, Germany). Four retroreflective spherical markers are each attached to the laparoscope's camera head, the laparoscope's cylindric shaft [cf. Fig. 6(c)], and a pointer [cf. Fig. 3(a)]. We utilize a helical BB phantom for geometric C-arm calibration (BB is a metal sphere), as shown in Fig. 3(b). The operating table is made of carbon in order to limit imaging artifacts during surgery.
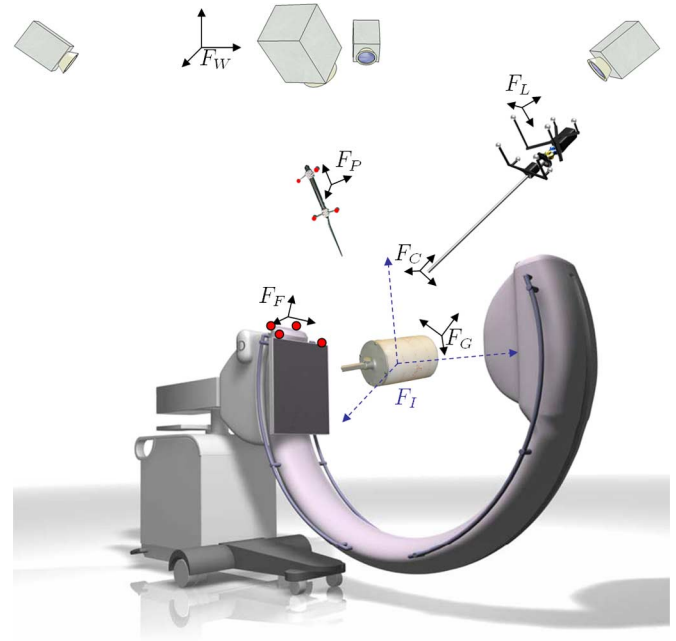
B. System Calibration

In order to augment C-arm data on the laparoscopic view, data represented in different coordinate systems (cf. Fig. 2) need to be brought into one common world coordinate system, e.g., tracking coordinate system. Therefore, two main transformations need to be computed. 1) The transformation from the markers attached to the laparoscope's body to the camera center along with the projection geometry of the laparoscope camera. 2) The transformation from the markers attached to the flat-panel detector to the isocenter of the C-arm. All calibration steps can be done offline. Their results are valid for a long period of time and only need to be repeated once in a while, as long as the marker targets on the C-arm and the laparoscope are not repositioned.

Repositioning, however, is an important issue, especially during sterilization. Practical commercial solutions already exist for the intraoperative use of markers attached to a mobile C-arm, like the system we actively use in our operating room (see Section I-B). For the sterilization of the laparoscope and its attached marker targets, autoclavable frames could be manufactured, which can be removed before sterilization and precisely reattached to the laparoscope afterwards. We currently use frames manufactured from laser-range scanning data, which precisely fit the head and shaft of the laparoscope. Screws firmly fix the markers as well as the frames. We will however replace all screw connections by snap-on connections in the future, as offered for instance by NDI[4] for their passive markers.

It is easy to setup on-site accuracy verification procedures to monitor the validity of all estimated parameters by imaging and superimposing volumetric data of an optically tracked phantom with known geometry on the laparoscopic view. This verification can be performed by a nurse or by the surgical staff in the
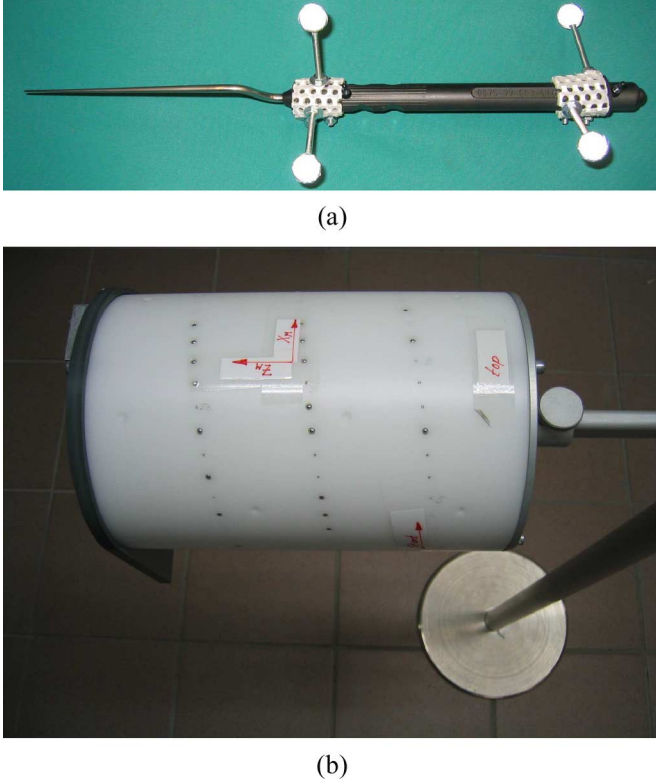
---

[4]http://www.ndigital.com/

(a)

(b)

Fig. 3. Calibration utensils used for C-arm calibration. (a) Pointer. (b) Hollow, cylindrical plastic phantom containing a helical pattern of BBs of two different diameters.

(a)

(b)

Fig. 4. Detailed illustrations of flat panel and evaluation phantom. (a) Marker target attached to the flat-panel detector of the C-arm. (b) Cubic evaluation phantom containing cylindrical bore holes of varying depth.

operating room before patient anesthesia. In case of unsatisfactory validation results a system recalibration may be performed on site, similarly to the approach of Falk *et al.*, where an interactive calibration of an endoscope was performed in three to eight minutes [9].

1) Pointer Calibration: For C-arm calibration (cf. Section II-B-3), a tracked pointer is used, which is illustrated in Fig. 3(a). Therefore, the pointer's tip position in its local target coordinate system needs to be determined first. This can be done by fixing the tip inside an indentation and recording tracking data, while the pointer is pivoted around its tip describing a hemisphere. Hence, a series of $i = 1 \ldots m$ translational and rotational measurements are acquired, which represent the transformation from pointer target coordinates into world coordinates. For each transformation ${}^W T_{P(i)}$, the pointer's tip remains static in pointer coordinates (X_P) as well as world coordinates (X_W), as described by following formula:
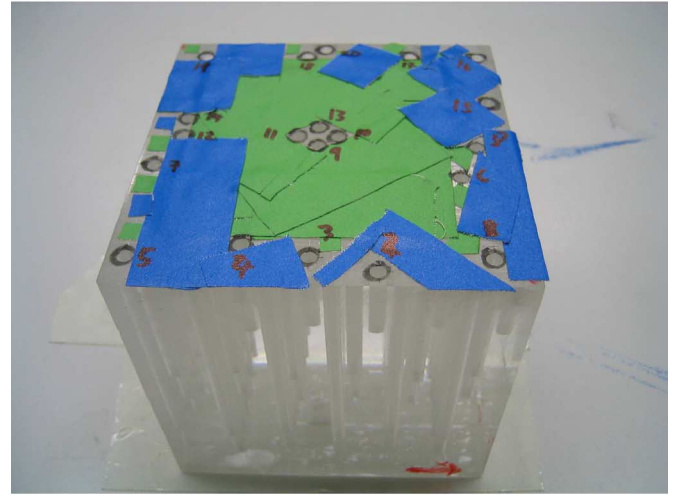
$$X_W = \left[{}^W R_{P(i)}\right] X_P + {}^W t_{P(i)}. \tag{1}$$

As depicted by Tuceryan *et al.* [30], following equation needs to be solved (e.g., by QR decomposition) to determine the pointer tip coordinates:

$$\begin{pmatrix} I & -\left[{}^W R_{P(1)}\right] \\ I & -\left[{}^W R_{P(2)}\right] \\ \vdots & \vdots \\ I & -\left[{}^W R_{P(m)}\right] \end{pmatrix} \begin{pmatrix} X_W \\ X_P \end{pmatrix} = \begin{pmatrix} {}^W t_{P(1)} \\ {}^W t_{P(2)} \\ \vdots \\ {}^W t_{P(m)} \end{pmatrix}. \tag{2}$$

2) Laparoscope Calibration: Two marker targets are rigidly attached to the laparoscope: one to the cylindrical shaft and another one to the camera head. The main purpose of calibrating the laparoscope is to model the transformation of a 3-D world point onto the camera's 2-D image plane, so the projection of any 3-D world scene onto the laparoscope's image can be modeled mathematically.

In detail, a point X_W in the world frame is first transformed into the laparoscope frame by ${}^L T_W$, from where it is transformed into the camera frame by ${}^C T_L$, and finally mapped onto the image plane by the camera calibration matrix K. x is the final 2-D point on the image plane

$$\begin{bmatrix} X_C \\ 1 \end{bmatrix} = \left({}^C T_L\right) \left({}^L T_W\right) \begin{bmatrix} X_W \\ 1 \end{bmatrix} \tag{3}$$

$$\begin{bmatrix} x \\ 1 \end{bmatrix} = K X_C, \text{ where } K = \begin{bmatrix} \alpha_x & & x_0 \\ & \alpha_y & y_0 \\ & & 1 \end{bmatrix}. \tag{4}$$

The transformation ^LT_W can be directly received from the tracking system. The transformation ^CT_L from laparoscope target to camera coordinate frame and the intrinsic camera parameters stored in K, i.e., focal length (α_x, α_y) and principal point (x_0, y_0), need to be computed once [31], [32]. Additionally, the rather large radial and tangential lens distortion of laparoscopes needs to be corrected for. While being required for a perfect augmentation, undistorted images are also preferred by surgeons [33]. To determine these parameters, a planar checkerboard pattern with 8×7 squares of 10 mm unit length is used. The pattern is viewed from several arbitrary poses $j = 1 \ldots n$, $n > 2$ satisfying distinct rotation axes for all possible motions between them [12]. It must be ensured that the laparoscope shaft is not rotated against the camera head during these movements. For each pose, an image is recorded along with the 6-D pose data provided by the tracking system. In each image, the inner corners of the checkerboard pattern are found automatically guaranteeing sub-pixel accuracy, giving a set of 42 sorted 2-D points.[5] Knowing their corresponding 3-D position on the pattern, the intrinsic camera parameters and distortion coefficients can be computed using well-established camera calibration techniques [34], [35]. An implementation can be found e.g., in the Open Source Computer Vision Library.[6]

Hand–eye calibration: The camera calibration algorithms also compute the transformations $^CT_{B(j)}$ of pattern coordinate frame F_B to camera frame. Each of them has a respective 6-D pose $^WT_{L(j)}$ that is acquired by the tracking system. Two of them can be each paired to a motion $T_{C(l \leftarrow k)} = [^CT_{B(l)}][^CT_{B(k)}]^{-1}$ and $T_{L(l \leftarrow k)} = [^LT_{W(l)}][^LT_{W(k)}]^{-1}$, respectively, giving $n(n-1)/2$ possible motions for the camera center as well as the laparoscope target. One motion pair gives following equation:

$$\left[T_{C(l \leftarrow k)} \right] \left[^CT_L \right] = \left[^CT_L \right] \left[T_{L(l \leftarrow k)} \right]. \qquad (5)$$

Stacking up all equations, the so-called hand–eye formulation $AX = XB$ can be formalized, where $X = [^CT_L]$. This can be solved for instance by first computing the rotational and then the translational part of X by QR decomposition [36] or by a dual quaternions approach [37], which both give similar results in terms of accuracy [38]. The transformation from the checkerboard to the world coordinate frame ^WT_B can be computed similarly using the same $j = 1 \ldots n$ poses $^CT_{B(j)}$ and $^WT_{L(j)}$, respectively.

Oblique scope calibration: ^CT_L will only remain static, if either a $0°$ laparoscope is used or a $30°$ one with the scope shaft not being rotated around its longitudinal axis against the camera head. However, especially for abdominal surgery the shaft of the frequently used $30°$ laparoscope is often rotated, invalidating the rigid transformation ^CT_L. Any rotational offset needs to be corrected for. We thus attached a second marker target to the scope shaft to measure its rotation against the camera head. Mathematically, this single rotation can be modeled by two successive mathematical rotations, as proposed by Yamaguchi *et al.* [39].

Therefore, first the camera and hand–eye calibration is performed keeping the scope shaft fixed at an initial constant rotation angle 0. This results in an initial transformation $^CT_{L(0)}$. To incorporate the laparoscope rotation into the final transformation ^CT_L, two mathematical rotations that are multiplied by the initial transformation are modeled: 1) The inverse rotation around the longitudinal axis of the shaft (shaft rotation $T_{Cs}(-\phi)$) by the rotation angle $-\phi$, 2) the rotation around the principal axis described by the viewing direction of the laparoscope (principal rotation $T_{Cp}(\phi)$) by ϕ. The following equation gives the overall transformation from the camera center to the laparoscope markers:

$$^CT_L = T_{Cp}(\phi) T_{Cs}(-\phi)\, ^CT_{L(0)}. \qquad (6)$$

Since in reality both rotation axes are not perfectly aligned with the longitudinal and principal axis, respectively, they need to be estimated.

The shaft rotation axis is determined by performing a full $360°$ rotation while measuring the 3-D positions of the tracking target attached to the laparoscope shaft. These measurements are transformed by $^CT_{L(0)}$ into the camera coordinate frame, wherein a circle can be estimated. The center of the circle corresponds to the origin, the normal to the plane described by the circle corresponds to the directional vector of the shaft axis [39].

The principal rotation axis can be computed acquiring images of the checkerboard pattern at several poses $i = 1 \ldots m$, where the checkerboard pattern must not be moved between camera, hand–eye, and oblique scope calibration. Again, for each image at pose i, the 3-D position of the shaft target is measured to estimate its corresponding rotation angle. Additionally, at the same time the pose of the camera head target is measured and $j = 1 \ldots n$ sorted 2-D points $x_{(ij)}$ are automatically detected for each rotation angle. Using the initial laparoscope to camera transformation $^CT_{L(0)}$, the origin and directional vector of the principal rotation axis can be computed by minimizing following equation using Levenberg-Marquardt:

$$\sum_{i=1}^{m} \sum_{j=1}^{n} \left\| K \left[R_{Cp}\left(\phi_{(i)}\right) \middle| t_{Cp}\left(\phi_{(i)}\right) \right] T_{Cs} \right.$$
$$\left. \times \left(-\phi_{(i)}\right) {}^CT_{L(0)}\, {}^LT_{W(i)}\, {}^WT_B \begin{bmatrix} X_{B(j)} \\ 1 \end{bmatrix} - \begin{bmatrix} x_{(ij)} \\ 1 \end{bmatrix} \right\|^2 \qquad (7)$$

3) C-Arm Calibration: The computation of the transformation ^FT_I from the isocenter to the flat panel coordinate frame is performed in two steps. First, the transformation ^IT_G from the calibration phantom's coordinate frame to the isocenter frame is determined during geometric calibration of the cone-beam CT capable C-arm, second the transformation ^WT_G from the phantom to the world coordinate frame.

For geometric C-arm calibration, we use the manufacturer's phantom and software [40]. A helical pattern of BBs of two different diameters inside a hollow, cylindrical plastic phantom is utilized, as visualized in Fig. 3(b). The center of each BB is known very precisely in 3-D in its local coordinate frame F_G. The geometric calibration is used to determine the reproducible non-ideal orbit of the C-arm around the scan volume. For every pose of the C-arm source (X-ray tube) and its corresponding

---

[5]A checkerboard pattern with 8×7 squares has exactly $7 \cdot 6 = 42$ inner corners.

[6]http://www.intel.com/technology/computing/opencv/

X-ray image across the orbit (detected on the flat panel), it determines the associated projection matrix. Knowing all projection matrices, a rigid transformation from the geometric calibration phantom's coordinate frame to the isocenter $^{I}T_{G}$ can be estimated.

The last missing transformation from the phantom coordinate frame to the world coordinate frame $^{W}T_{G}$ is then estimated as in Ritter *et al.* [41]. The tracked pointer is used to acquire the 3-D coordinates of the BBs' outward surface on the phantom in the world coordinate frame. To compensate for the fact that the pointer only touches the surface of a BB and not its center, an offset needs to be added to each BB's coordinate. This offset equals a BB's radius and is along the orthogonal to the tangent touching the surface of the phantom.

By matching the coordinates of the point set acquired with the pointer and the corresponding BBs' adjusted coordinates in the calibration phantom, the unknown transformation can be computed e.g., by applying singular value decomposition.

C. Visualization

Our navigation workstation is equipped with 2 GB main memory, an Athlon 64 3500+ CPU, and an NVIDIA GeForce 6800 Ultra graphics card with 256 MB memory. The reconstruction software of the C-arm generates a 16 bit gray level volume of $512 \times 512 \times 384$ voxels. Using the CG shader language,[7] we are able to directly render this volume in real time as view-aligned 3-D textures. We augment the volume rendering directly on the live laparoscope video. The originally distorted laparoscope images are undistorted in real time as well. To visualize certain tissues only, specific colors and opacities can be interactively assigned to the rendered textures, provided by a graphical transfer function editor. Alternatively, default transfer functions can be loaded, for instance tailored to contrasted vessels. To easily synchronize tracking with video data and visualize the augmentation, we use our medical augmented reality framework CAMPAR [42].

III. AUTOMATED 3-D RECONSTRUCTION FOR PATIENT REGISTRATION DURING PORT PLACEMENT

For patient registration needed for port placement, three essential steps are required. 1) All fiducials must be segmented in the CT volume to determine the positions of their centroids. 2) Their positions in the world coordinate frame need to be reconstructed using the images, which are acquired by the calibrated laparoscope camera and show the fiducials. 3) The resulting point sets need to be matched in order to register the patient to the CT data set.

The automatic segmentation of the fiducials in the CT volume can be achieved by using standard image processing techniques based on thresholding, filling, morphology, and subtraction [43], [44]. The centroids of all segmented fiducials can be computed very precisely by weighing their associated voxel intensities and incorporating partial volume effects.

For finding the 3-D positions of the fiducials in the world coordinate frame, two iterations are performed for each image i containing an arbitrary number m of fiducials. First, the 2-D

positions $x_{(i1)} \ldots x_{(im)}$ of all visible fiducials are extracted automatically after undistortion of the image. Similar techniques as for the segmentation of the CT data are used, which also incorporate edge detection and color information of the fiducials and patient's skin [44]. Second, the epipolar geometry is used to match and reconstruct their 3-D positions as follows.

For each image i, the laparoscope camera's extrinsic parameters, meaning the transformation $^{C}T_{W(i)}$ from world to camera coordinate frame can be computed

$$^{C}T_{W(i)} = {}^{C}T_{L} {}^{L}T_{W(i)}. \tag{8}$$

Thus, for each image pair i and j, the transformation between its associated camera poses, $T_{C(j \leftarrow i)}$, and its corresponding essential matrix $E_{(j \leftarrow i)}$ can be computed [45]

$$T_{C(j \leftarrow i)} = \begin{bmatrix} R_{C(j \leftarrow i)} & t_{C(j \leftarrow i)} \\ 0 & 1 \end{bmatrix}$$
$$= {}^{C}T_{W(j)} \left({}^{C}T_{W(i)} \right)^{-1} \tag{9}$$
$$E_{(j \leftarrow i)} = \left[t_{C(j \leftarrow i)} \right]_{\times} R_{C(j \leftarrow i)}$$

$$\text{where} \quad [t]_{\times} = \begin{bmatrix} 0 & -t_z & t_y \\ t_z & 0 & -t_x \\ -t_y & t_x & 0 \end{bmatrix}. \tag{10}$$

Since the camera is calibrated, all epipolar lines $(l_{C(j)})_1 \ldots (l_{C(j)})_m$ in image j corresponding to the points in image i can be determined

$$\left(l_{C(j)} \right)_k = K^{-T} E_{(j \leftarrow i)} \left(X_{C(i)} \right)_k$$
$$\text{where} \quad \left(X_{C(i)} \right)_k = K^{-1} \begin{bmatrix} \left(x_{C(i)} \right)_k \\ 1 \end{bmatrix}. \tag{11}$$

If any of the points in image j lies on an epipolar line or very close to it (e.g., within one pixel), it is very likely that this point and its corresponding point in image i are projections of the same 3-D point. So this point is reconstructed by computing the intersection of the two rays back-projected from $\left(X_{C(i)} \right)_k$ and $\left(X_{C(j)} \right)_l$, respectively. However, since the camera's intrinsic and extrinsic parameters were only estimated during calibration and tracking, the two rays will not exactly intersect in space. Hence, the midpoint of the two rays is computed by determining their intersection points with the segment that is orthogonal to both rays, which can be achieved by solving a linear system of equations [46]

$$t_{C(i \leftarrow j)} = a \left(X_{C(i)} \right)_k - b R_{C(i \leftarrow j)} \left(X_{C(j)} \right)_l$$
$$+ c \left(\left(X_{C(i)} \right)_k \times \left(R_{C(i \leftarrow j)} \right) \left(X_{C(j)} \right)_l \right) \tag{12}$$

where $R_{C(i \leftarrow j)} = (R_{C(j \leftarrow i)})^T$ and $t_{C(i \leftarrow j)} = -(R_{C(j \leftarrow i)})^T t_{C(j \leftarrow i)}$. The intersection points in the camera coordinate frame now are $a(X_{C(i)})_k$ and $t_{C(i \leftarrow j)} + b(R_{C(i \leftarrow j)})(X_{C(j)})_l$, so their midpoint can be easily computed and transformed into the world coordinate frame, as described by following equation:

$$\begin{bmatrix} X_W \\ 1 \end{bmatrix} = \left({}^{C}T_{W(i)} \right)^{-1}$$
$$\times \begin{bmatrix} \left(a \left(X_{C(i)} \right)_k + t_{C(i \leftarrow j)} + b \left(R_{C(i \leftarrow j)} \right) \left(X_{C(j)} \right)_l \right) / 2 \\ 1 \end{bmatrix}. \tag{13}$$

Wrong reconstructions can always happen, if a point close to or on the epipolar line is found, which actually corresponds to another point than the one the epipolar line belongs to. The following approach is taken to identify incorrect reconstructions. The fiducials are positioned at a minimum distance of 30 mm. Therefore, all reconstructed points having a certain maximal distance, e.g., are closer to each other than 10 mm, are assumed to represent the same point in 3-D. For each such 3-D point, its corresponding 2-D point pairs are combined into a list. All lists are compared to each other. If a 2-D point happens to be in more than one list, its corresponding point pair is kept in the list with most point pairs and deleted from all other lists. By validating lists with more than two point pairs only, 3-D points can be reconstructed with the utmost probability.

In the next reconstruction step, the lists with point pairs corresponding to the same 3-D point are used to optimally reconstruct the 3-D point. For all 2-D points, their associated projection rays $r_1 \ldots r_s$ are constructed, which intersect the camera center $C_r = {}^W t_{C(i)}$ and the point's projection onto the image plane $P_r = {}^W R_C^i (X_{C(i)})_k + {}^W t_{C(i)}$, where ${}^W R_{C(i)} = ({}^C R_{W(i)})^T$ and ${}^W t_{C(i)} = -({}^C R_{W(i)})^T {}^C t_{W(i)}$. They can be represented using the camera center C_r as starting point and a directional unit vector $d_r = (P_r - C_r)/\|P_r - C_r\|$

$$r_r = C_r + \lambda_r d_r = C_r + \lambda_r \frac{P_r - C_r}{\|P_r - C_r\|}. \tag{14}$$

Again, the associated midpoint X_w can be computed, which is closest in average to all s rays. Therefore, following overdetermined system of linear equations has to be minimized:

$$\sum_{r=1}^{s} \|C_r + \lambda_r d_r - X_w\|^2. \tag{15}$$

As stated by Sturm et al., this linear least squares problem may be solved using the Pseudo-inverse [47]

$$
\begin{bmatrix} X_W \\ \lambda_1 \\ \vdots \\ \lambda_s \end{bmatrix} =
\begin{bmatrix} nI & -d_1 & \cdots & -d_s \\ -(d_1)^T & 1 & & \\ \vdots & & \ddots & \\ -(d_s)^T & & & 1 \end{bmatrix}^{-1}
$$
$$
\times \begin{bmatrix} I & \cdots & I \\ -(d_1)^T & & \\ & \ddots & \\ & & -(d_s)^T \end{bmatrix}
\begin{bmatrix} C_1 \\ \vdots \\ C_s \end{bmatrix}. \tag{16}
$$

Finally, these results can be further improved by using the Levenberg-Marquardt iteration to minimize following equation:

$$\sum_{r=1}^{s} \left\| K \begin{bmatrix} {}^C R_L \vert {}^C t_L \end{bmatrix} ({}^L T_W)_r \begin{bmatrix} X_W \\ 1 \end{bmatrix} - \begin{bmatrix} x_r \\ 1 \end{bmatrix} \right\|^2 \tag{17}$$

It must be noted that our reconstruction approach solves the general case that several fiducials are visible in a single laparoscope image but some may be missing, similar to the work of Nicolau et al. [18], where two stationary cameras are used to provide a stereo view of fiducials. We implemented this general approach in order to remain flexible with respect to the utilized camera or endoscope. Future advances of digital and high-definition endoscopes may provide us with a laparoscope camera, which is able to see several fiducials at the same time with a very high resolution. However, we currently have a laparoscope with an analog camera and therefore utilize a more restricted reconstruction protocol. The laparoscope is hold close to a fiducial, so that no other fiducial can be seen at the same time, and is pivoted around this fiducial. The fiducial is segmented in each image and its position is added to a list of 2-D points, which is in turn used to reconstruct the fiducial's 3-D position, as described above. This process is repeated for all other fiducials.

After the reconstruction of all 3-D points from the 2-D points of their associated lists, they need to be matched with the points segmented in the CT data set. Therefore, the correct point correspondences need to be identified and the transformation from the CT coordinate frame into the world coordinate frame, where the patient is registered in, needs to be computed. This can be done by a distance-weighted graph matching approach along with a point based registration algorithm [48], [49]. Finally, the patient's CT volume is registered in the same coordinate frame as the patient.

An alternative approach for the computation of this final registration, which considers noise in 2-D as well as in 3-D data, was introduced by Nicolau et al. [50]. Based on radio-opaque fiducials, they propose an extended 3-D/2-D criterion to register a 3-D model generated from preoperative CT data to the patient for augmented reality guided radio frequency ablation.

IV. ACCURACY EVALUATION

The major contributor to the overall system error is the optical tracking system in use. A typical setup with four ART cameras has a root mean square (rms) error of 0.4 mm for the target position and $0.12°$ for the target orientation and a maximum error of 1.4 mm for positional and $0.4°$ for orientational measurements.[8]

In our previous work, an average error of 2.6 mm on a rigid phantom was proven to be more than adequate for port placement [12]. To evaluate the overall system accuracy during *in situ* resection planning, we performed two types of experiments. First, the navigation accuracy with the tracked pointer was assessed, second the augmentation accuracy using the tracked laparoscope.

It must be noted that registration-free C-arm-based 3-D navigation systems are commercially available and used in neurosurgery, orthopedics and trauma surgery routinely on a daily basis. As for our proposed system, both the C-arm and surgical instruments are optically tracked during surgery. The accuracy of such a registration-free C-arm-based navigation system was evaluated to be better than 2 mm for pedicle screw placement [51], [52], making it superior to conventional approaches or CT-based navigation procedures, where anatomical landmarks are required to register the patient to its preoperative CT volume set.

A. Navigation Error

To determine the overall system's navigation accuracy, we used the cubic evaluation phantom developed by Ritter et al. that

---

[8]Accuracy of a typical ART tracking system available at http://www.art-tracking.de.

contains cylindrical bore holes of varying depth [41], as shown in Fig. 4(b). The phantom was adhered to the operating table with double-sided adhesive tape. Then the varying depth of 20 bore holes was measured in terms of the pointer tip's 3-D position in the tracking coordinate system. The bottom of all bore holes could be entirely reached, as the pointer has a sharp tip. The measured tip coordinates were transformed into the volume coordinate system by ${}^{I}T_{F}{}^{W}T_{F}{}^{-1}$. Now each of the 20 bore holes was filled with a single BB of radius $r = 1.5$ mm. Afterwards, a volume was reconstructed, wherein the BBs' centroids were extracted automatically by a hybrid segmentation algorithm based on thresholding, region growing, the BBs' shape, and weighing of voxel intensities.

Since the bore holes have an inclination α of 56°, the distance from a BB's centroid to the end of the bore hole equals $r/\cos\alpha$. This distance offset needs to be applied to all segmented centroids to be theoretically aligned with the tip of the pointer.

The overall Euclidean rms error between the measured and segmented coordinates of the BBs' centroids was 1.10 mm, which confirms previous results of Ritter *et al.* [41]. A second experiment after a complete system recalibration using BBs of 1.0 mm radius resulted in a reproducible Euclidean rms error of 1.05 mm.
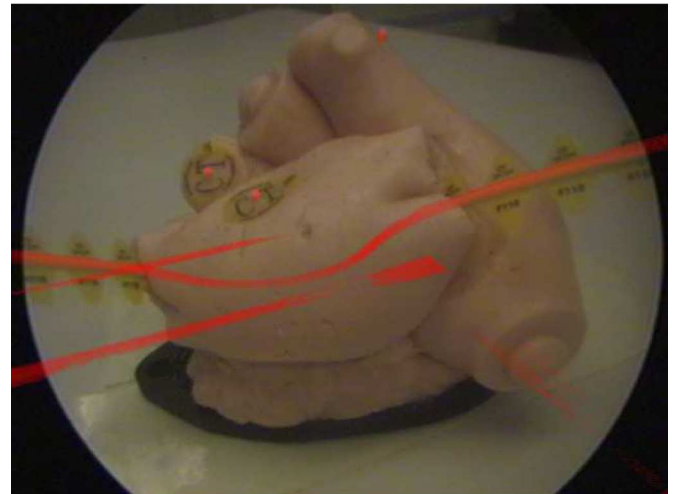
B. Augmentation Error

For the determination of the laparoscopic augmentation error, a volume of a plastic model of a heart with three adhered spherical fiducials of 2.3 mm diameter and a curved line marker (CT-SPOTS, Beekley Corporation, Bristol, CT) representing a vessel was reconstructed. The laparoscope was moved around this plastic model arbitrarily. Augmenting the live laparoscope video, images were taken from a large number of views covering the interventional working space. On all images the fiducials and their augmented counterparts, visualized in a different color, are visible (cf. Fig. 5). The absolute distance in mm was measured from the midpoint of a spherical fiducial and its corresponding virtual projection. The obtained rms error was 1.78 mm, the maximum error 4.14 mm, and the standard deviation (SD) 1.12 mm. This high error was caused by an inappropriate configuration of the markers on our laparoscope [cf. Fig. 6(a)], leading to unstable tracking, e.g., by partial or complete occlusions of the markers. This behavior could be anticipated, since the calibrated camera center is located about 350 mm away from the markers, leading to a large extrapolation displacement for small angular or translational tracking errors of the markers.

Therefore, in a second experiment we rearranged the four markers on the laparoscope, so they could be seen optimally by the tracking system in almost every possible position [cf. Fig. 6(b)], following the heuristics described by West and Maurer [53]. For a detailed description of the equations and errors involved in tracking distal tips of long instruments and optimal marker design refer for example to recent results presented by Fischer and Taylor [54] as well as Bauer *et al.* [55]. After a recalibration of the laparoscope, we were able to significantly improve the augmentation accuracy from all positions of the laparoscope and could decrease the rms error

(a)

(b)

Fig. 5. Plastic heart used for the determination of the augmentation error. (a) Real, undistorted laparoscope image showing the three spherical fiducials and a curved line marker on the plastic heart. (b) Augmented laparoscope image. Volume rendered are only the fiducials; the additional lines are artifacts in the reconstructed volume.

to only 0.81 mm, the maximum error to 1.38 mm, and the SD to 0.44 mm.

During surgery, however, the full flexibility of the laparoscope is required to change viewing directions, i.e., the laparoscope shaft shall be able to be freely rotated against the camera head. Hence, two new marker targets were designed and attached to the laparoscope [cf. Fig. 6(c)]. After recalibration, the augmentation accuracy when rotating the laparoscope head was determined. The rms error was 1.58 mm, the maximum error 2.81 mm, and the SD 0.74 mm.

V. EXPERIMENTS

To clinically evaluate our laparoscope augmentation system for port placement planning and liver resection planning, we performed three kind of experiments together with our clinical partners: offline port placement, *ex vivo*, and *in vivo* studies.

(a)   (b)   (c)
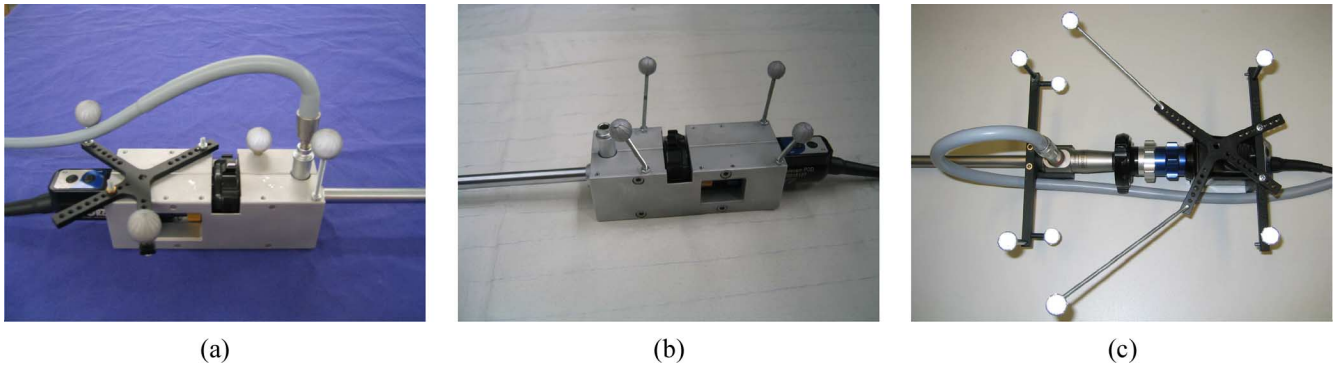
Fig. 6. Several developed marker target configurations—according to the surgeons, they are not disadvantageous for the laparoscope handling and comfort. (a) Initial suboptimal marker configuration. (b) Rearranged markers to ensure optimal tracking properties. (c) Two marker targets to track the laparoscope rotation.
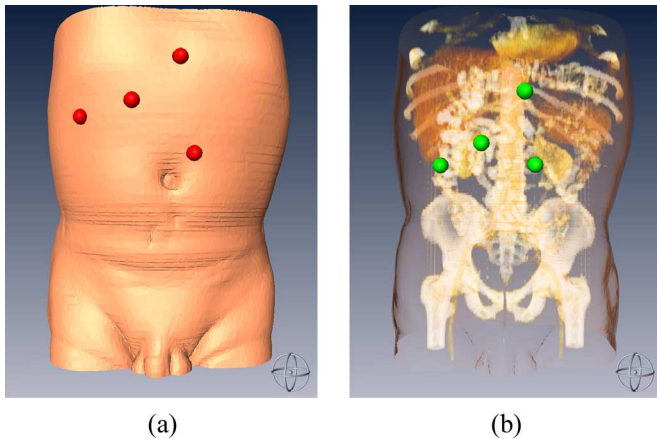

(a)   (b)

Fig. 7. Offline port placement experiments. Four ports were chosen using two different visualization modes. Both views are from the same perspective. (a) Three-dimensional view of the skin. (b) Transparent 3-D view.

A. Offline Port Placement Studies

To evaluate our visualization system for port placement, we conducted a first series of offline experiments on human and porcine CT data. For the human data set, we chose a typical venous CT data set, for the porcine data set we chose one of the two data sets acquired for our *in vivo* experiments (cf. Section V-C). Four surgeons, who are all experienced in laparoscopic surgery, were asked to place four typical ports for liver resection (one laparoscope and three instrument ports), based on two different visualization modes, which were shown consecutively. In the first mode [cf. Fig. 7(a)], only orthogonal 2-D slices and a 3-D view of the skin were shown to the surgeons to simulate their conventional way of placing ports (except for palpation). In the second mode [cf. Fig. 7(b)], the skin was made transparent, so the surgeons were able to see the abdominal interior, based on the previously described visualization techniques (cf. Section II-C). To independently place a set of four ports in each data set, the surgeons simply had to click inside the 3-D view.

We calculated the Euclidean 3-D distances between corresponding ports chosen with the first and the second visualization method. For the patient data set, distances between 6.57 mm and 66.20 mm were computed with an rms of 40.42 mm and an SD of 17.59 mm. For the pig, the distances were between 6.38 mm and 48.74 mm with an rms of 22.28 mm and an SD of 11.07 mm. Although the distances of corresponding ports in

the porcine data set seem to be much smaller, for a direct comparison they would need to be scaled, as the pig was relatively young (3–6 months, 16–20 kg), while the patient was adult.

In comparison to the standard port placement technique, our visualization aid considering individual patient anatomy significantly altered port placement both in human and animal data sets. All surgeons agreed that our visualization method supports the surgical procedure and port placement accuracy.

B. Ex Vivo Perfusion Studies

The second series of experiments was conducted on a freshly harvested whole porcine liver and a defrosted whole ovine kidney. In both cases, we placed the organ in a perfusion box (Pulsating Organ Perfusion Trainer, OPTIMIST Handelsges.m.b.H., Bregenz, Austria). The surgeons catheterized the liver's portal vein and the kidney's renal artery, respectively. Then the iodinated nonionic contrast agent SOLUTRAST 300 was administered into the organ. It was diluted in normal saline and conveyed into the organ by the pump of the perfusion system. We immediately started a C-arm acquisition and reconstructed the organs's 3-D volume. In another experiment, we directly injected the pure contrast agent.

The acquisition of 200 C-arm projections takes 64 s, which stays within the time limits of holding breath during artificial respiration. Alternatively, 100 projections can be acquired, which only takes 32 s. After acquisition, the reconstruction of the 3-D volume was started, which currently takes about 6 min for 200 projections or 3 min for 100 projections, respectively. The reconstruction software, which is provided by Siemens Medical, was uncoupled from the overall software package to allow better control and debugging of the reconstruction process. However, once the prototype system is commercialized, the reconstruction algorithms will be further optimized and parallelized. Additionally, reconstruction will commence as soon as the first projection is acquired. This will lead to reconstruction times of approximately one minute after completion of a scan, as known from modern flat panel based angiographic computed tomography (ACT) scanners such as the DynaCT, where a volume set is available for assessment in less than 3 min.[9]

The contrasted part was clearly visible in the reconstructed volume for both cases, directly as well as via the perfusion
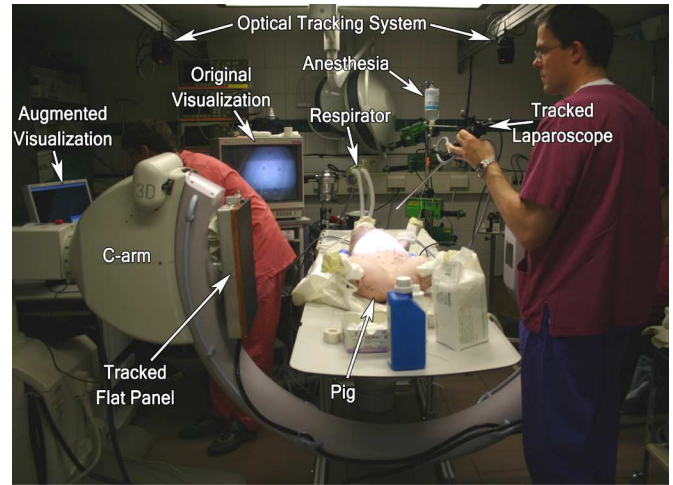
[9]http://www.healthcare.siemens.com/dynact/
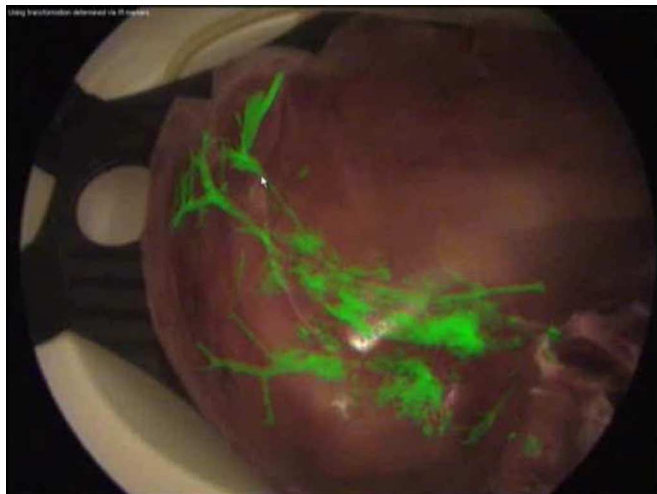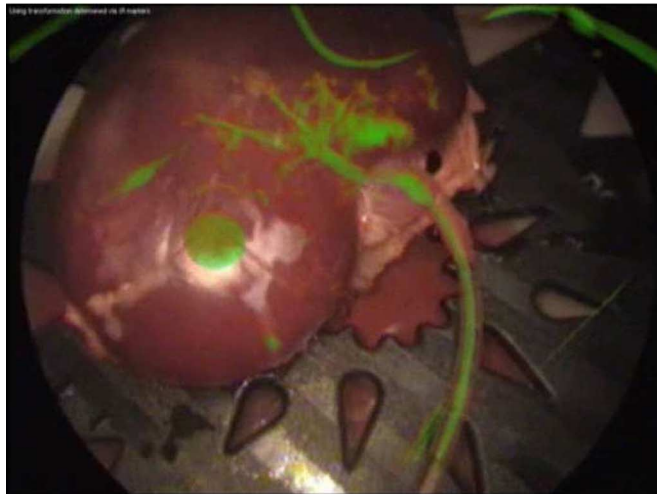
Fig. 8. *Ex vivo* vessel augmentation. (a) Augmented porcine liver. Speckled areas are reconstruction artifacts caused by a high concentration of contrast agent. (b) Augmented ovine kidney. Big spot is the perfusion system's plug, which apparently has a similar Hounsfield unit like the contrast agent.

Fig. 9. *In vivo* port placement. (a) Tracked laparoscope defines the viewing direction of the virtual visualization along the instrument axis. (b) Virtual visualization enables the surgeon to see important anatomy—annotations added manually (note that these are static frames of dynamic video sequences, which provide better perception of anatomical structure to the surgeons).

system. The vessels were directly augmented on the laparoscope's view by volume rendering, which utilizes predefined transfer functions in such a way that only voxel intensities of the contrast agent are rendered. This direct visualization technique does not require any processing time, since time-consuming segmentation, as it would be needed for surface-based rendering, can be completely avoided. The vessels could be accurately overlaid for most laparoscope positions, as one can see in Fig. 8(b) in the case of the kidney, where the real and virtual catheters appear to perfectly overlap. In the case of the porcine liver, only the vessels of one lobe could be contrasted partially, as some liver vessels were accidentally cut at the abattoir.

Although in general more vessels could be visualized for the direct administration of contrast agent, artifacts appeared during the 3-D volume reconstruction due to the high concentration. We will conduct further studies to find an optimal contrast agent concentration for an artifact-free reconstruction and a clear visualization of all relevant vessels.

C. In Vivo Porcine Studies

In a third series of experiments, we evaluated the overall system *in vivo* for both port placement and resection planning. Additionally, deviations from the correct augmentation caused by deformations of the liver due to breathing were analyzed.

For the *in vivo* studies, two live pigs of 16–20 kg were anesthetized by injections given in the auricular veins on the dorsal surface of the ears. Spherical fiducials were adhered to each pig's skin using DERMABOND adhesive (Ethicon GmbH, Norderstedt, Germany) to ensure their fixation during transportation of the pig. The fiducials were positioned on the abdominal wall in areas such that they are not moving too excessively during breathing. The pig was carried to the radiology department, where 50 ml contrast agent (SOLUTRAST 300) was administered at a flow of 3 ml/s. CT data was acquired in both arterial and venous phases. Four fiducials were segmented in the venous CT data set. Back in the animal operating room,
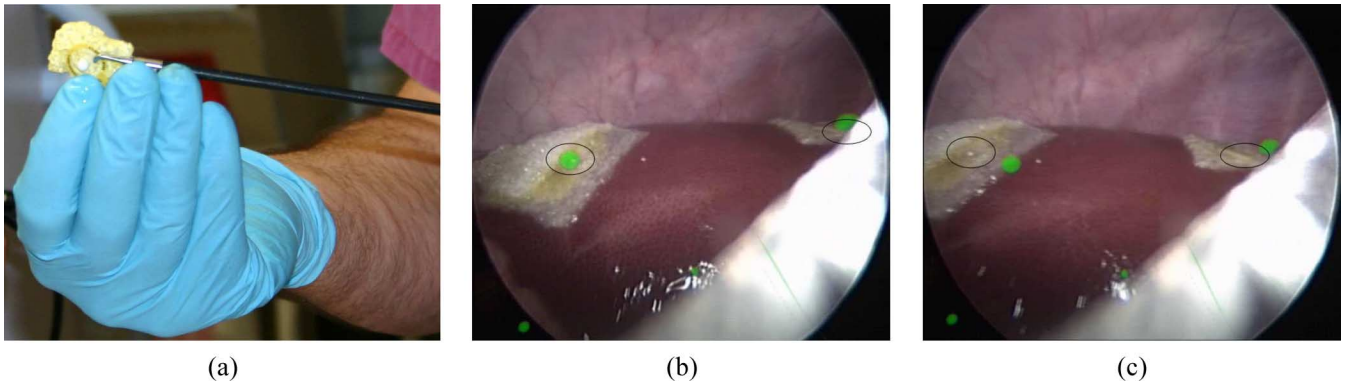
(a)   (b)   (c)

Fig. 10. Fiducials adhered to the liver surface—black ellipses added manually to outline the current (actual) fiducial positions. (a) Fibrin pad wrapped around a fiducial, which is glued to the liver surface. (b) Intrinsically registered augmented fiducials as seen during exhalation. (c) Displaced fiducials as seen during inhalation.

the pig was connected to an artificial respiration system to keep its breathing constant. The pig's vena jugularis was cannulated, so that it can be used for future contrast injections.

The tracked laparoscope was moved around the fiducials to reconstruct their 3-D positions, which took approximately 2 min. Matching them automatically to all fiducials previously segmented in CT, the pig could be registered to its venous CT data set. The CT data set was augmented directly on the laparoscope by means of direct volume rendering. Since the pig was placed in a different position than during the acquisition of the CT, the fiducials were displaced to a certain extent. Using four fiducials for registration, we calculated an rms error of 11.05 mm, a maximum error of 17.11 mm, and an SD of 4.03 mm, which complies with previous reports of Falk *et al.* [9]. Even though, due to the large displacement of the subject between preoperative and intraoperative imaging, the CT data set can not be used for a precise intraoperative augmentation during resection planning, it still fulfills the rather low accuracy requirements for port placement. This is due to the fact that patient's skin and hence inserted trocars can be moved about two centimeters to compensate for possible port displacements. Switching to a coregistered virtual visualization with 0° optics [cf. Fig. 9(b)], the bones and all contrasted sections such as aorta, kidneys, and hepatic veins were visualized in respect to the instruments' axis. All ports were planned successfully and the trocars could be placed appropriately (see surgeons' feedback at the end of this section).

After insufflation of CO_2, two spherical fiducials of 4 mm diameter were glued to the surface of the liver using a fibrin pad, as shown in Fig. 10(a). The artificial respiration system was temporarily turned off in exhalation. While injecting about 130 ml of contrast agent into the vena jugularis (and the auricular vein for the second pig, respectively), 100 orbiting C-arm projections were acquired at the same time, which took 32 s. A volume was reconstructed and transferred to the navigation workstation. As we used plastic trocars and removed all instruments for the scan, reconstruction artifacts could be largely avoided. Since laparoscope and C-arm are both coregistered in the tracking coordinate system, the transferred volume could be immediately augmented on the laparoscopic view. First, the movement of the liver caused by breathing was analyzed in the permanently augmented laparoscope images. As visualized on Fig. 10(b) and (c),
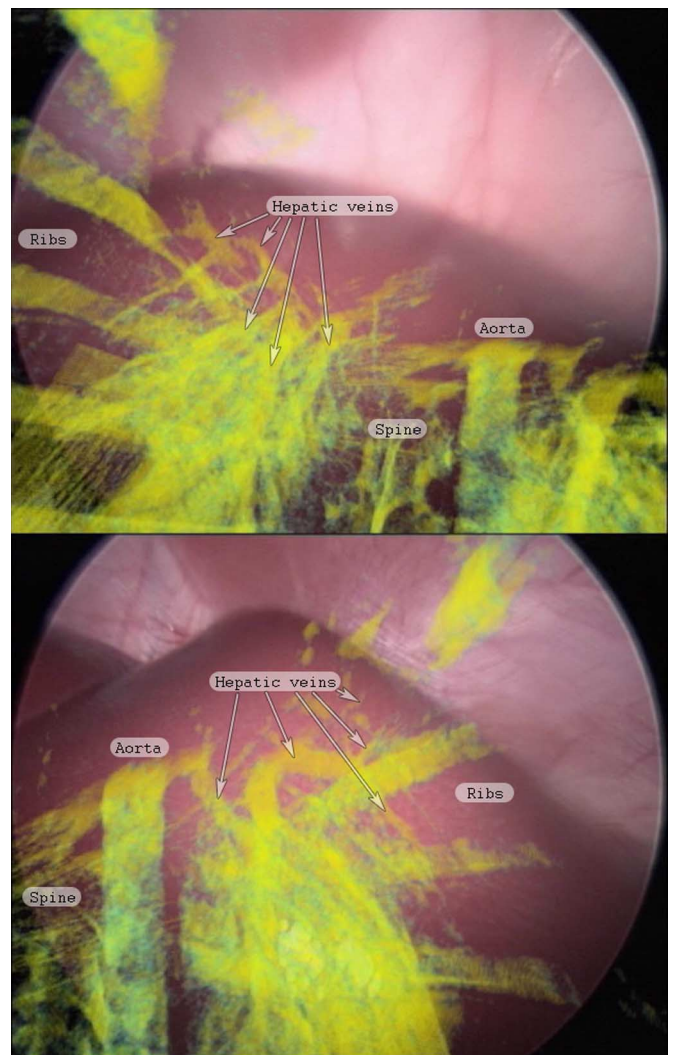

Fig. 11. *In vivo* laparoscopic augmentation of contrasted hepatic veins and aorta as well as ribs and spine—annotations added manually (again note that these are static frames of dynamic video sequences, which provide better perception of anatomical structure to the surgeons, who are used to look at 2-D laparoscopic projections during the operation).

a deformation of about 1 cm could be confirmed between exhalation and inhalation, as found previously by Herline *et al.* [14].

Consequently, our final augmentation error can be approximated to be between 2 mm (during expiration) and 12 mm (during inspiration), depending on the current respiratory phase. Next, the contrasted hepatic veins were augmented on the surface of the liver to plan the resection (cf. Fig. 11). After successful planning, the visualization was switched off and the surgeon started the resection.

Finally, the two participating surgeons were interviewed on the assets and drawbacks of our augmented visualization system. Both surgeons agreed on the successful validation of our visualization in an in vivo model. They confirmed that the augmentation for port planning is integrated smoothly and gives valuable as well as sufficiently accurate information on trocar placement. Since the contrast in the peripheral hepatic veins was too low, for the augmentation during liver resection planning only the major vessels could be visualized. Therefore, we need to further improve the timing and protocol of contrast agent administration, e.g., to reduce the amount of contrast agent to a maximum of 50 ml, which is the default dose for a human patient. This was expected, since this was one of the first experiments with intraoperative cone beam reconstruction of contrasted liver. The surgeons did not ask for the synchronization of the pig's respiration and pulse to the laparoscopic augmentation. Knowing that the augmentation is correct only at expiration, both surgeons claimed not to be distracted by the continuous augmentation during breathing. They were satisfied with the current augmented visualization, which could allow them to perform appropriate intraoperative resection planning. The surgeons however asked for intraoperative segmentation of the contrasted vessels so that the system can provide them with the exact (metric) positioning of tracked instruments relative to the vascular structure at the expiration.

VI. CONCLUSION

In this work we introduce the use of two independent intraoperative imaging systems, i.e., X-ray C-arm and laparoscopic camera within a registration-free navigation framework. By combining such intraoperative imaging, tracking, and visualization, we propose a method, which implicitly takes into account the organ movement between preoperative and intraoperative imaging. The system provides *advanced visualization for both port placement planning and intraoperative resection planning*. Our experiments and studies show satisfying qualitative results for improvement of intraoperative visualization in laparoscopic surgery.

The presented patient registration method for port placement planning, which is currently applied by pivoting the laparoscope around single fiducials to reconstruct their 3-D positions, is designed to also work when several fiducials are seen by the laparoscope at the same time. This is an important feature for prospective advances of high definition digital endoscope cameras that are able to provide high-resolution images of several or all fiducials, each of them easily and accurately detectable. Hence, a few distinct, but arbitrary views may be enough in the future, which saves time and makes the pivoting process dispensable.

Our system is not restricted to liver surgery. It may also be applied to various other endoscopic interventions, for instance to tumor resection procedures such as partial adrenalectomy, partial pancreatectomy (especially endocrine neoplasms in the pancreatic tail), and partial nephrectomy, or to stone removal procedures such as nephrolithotomy or percutaneous nephrostolithotomy, where C-arm fluoroscopic guidance is used anyway during stent placement, tract creation, calyceal puncture, stone localization, and placement of the nephrostomy tube. Our system is especially useful for difficult cases, where the tumor is embedded into the vessels (in close proximity to vessels) or located between the hepatic veins (segment VIII or IVa). These cases also justify additional radiation and contrast agent exposure—for other cases, preoperative CT or MRI may be sufficient.

The result provided here could allow different methods proposed in the literature [23], [24] to utilize coregistered intraoperative cone beam reconstruction in order to improve their advanced visualization solutions.

REFERENCES

[1] M. B. Thomas and A. X. Zhu, "Hepatocellular carcinoma: The need for progress," *J. Clin. Oncol.*, vol. 23, no. 13, pp. 2892–2899, 2005.

[2] T. Mala and B. Edwin, "Role and limitations of laparoscopic liver resection of colorectal metastases," *Digestive Diseases*, vol. 23, pp. 142–150, 2005.

[3] A. M. Chiu, D. Dey, M. Drangova, W. D. Boyd, and T. M. Peters, "3-d image guidance for minimally invasive robotic coronary artery bypass," in *Heart Surgery Forum*, 2000, vol. 3, no. 3, pp. 224–231.

[4] J. Traub, M. Feuerstein, M. Bauer, E. U. Schirmbeck, H. Najafi, R. Bauernschmitt, and G. Klinker, "Augmented reality for port placement and navigation in robotically assisted minimally invasive cardiovascular surgery," in *Comput. Assist. Radiol. Surg.*, Jun. 2004, pp. 735–740.

[5] L. Adhami and È. Coste-Manière, "Optimal planning for minimally invasive surgical robots," *IEEE Trans. Robot. Automat.*, vol. 19, no. 5, pp. 854–863, Oct. 2003.

[6] J. Cannon, J. Stoll, S. Selha, P. Dupont, R. Howe, and D. Torchiana, "Port placement planning in robot-assisted coronary artery bypass," *IEEE Trans. Robot. Automat.*, vol. 19, no. 5, pp. 912–917, Oct. 2003.

[7] J. Marmurek, C. Wedlake, U. Pardasani, R. Eagleson, and T. Peters, "Image-guided laser projection for port placement in minimally invasive surgery," in *Medicine Meets Virtual Reality 14: Accelerating Change in Healthcare: Next Medical Toolkit*, ser. Studies in Health Technology and Informatics. Amsterdam, The Netherlands: IOS Press, 2005, vol. 119, pp. 367–372.

[8] L. Adhami and È. Coste-Manière, "A versatile system for computer integrated mini-invasive robotic surgery," in *Proc. Int. Conf. Med. Image Computing Comput. Assist. Intervention (MICCAI)*, Tokyo, Japan, 2002, pp. 272–281.

[9] V. Falk, F. Mourgues, L. Adhami, S. Jacobs, H. Thiele, S. Nitzsche, F. W. Mohr, and È. Coste-Manière, "Cardio navigation: Planning, simulation, and augmented reality in robotic assisted endoscopic bypass grafting," *Ann. Thoracic Surg.*, vol. 79, pp. 2040–2047, Jun. 2005.

[10] S. D. Selha, P. E. Dupont, R. D. Howe, and D. F. Torchiana, "Dexterity optimization by port placement in robot-assisted minimally invasive surgery," in *Telemanipulator and Telepresence Technologies VIII*, ser. Proceeding of SPIE. Bellingham, WA: , Feb. 2002, vol. 4570, pp. 97–104.

[11] È. Coste-Manière, L. Adhami, F. Mourgues, and O. Bantiche, "Optimal planning of robotically assisted heart surgery: First results on the transfer precision in the operating room," *Int. J. Robot. Res.*, vol. 23, pp. 539–548, Apr.–May 2004.

[12] M. Feuerstein, S. M. Wildhirt, R. Bauernschmitt, and N. Navab, "Automatic patient registration for port placement in minimally invasive endoscopic surgery," Proceedings of the International Conference on Medical Image Computing and Computer Assisted Intervention (MICCAI) ser. Lecture Notes Comput. Sci., J. S. Duncan and G. Gerig, Eds., vol. 3750 New York, Springer-Verlag, 2005, pp. 287–294.

[13] B. Olbrich, J. Traub, S. Wiesner, A. Wiechert, H. Feußner, and N. Navab, "Respiratory motion analysis: Towards gated augmentation of the liver," in *Comput.Assist. Radiol. Surgery*, Berlin, Germany, Jun. 2005, pp. 248–253.

[14] A. Herline, J. Stefansic, J. Debelak, S. Hartmann, C. Pinson, R. Galloway, and W. Chapman, "Image-guided surgery: Preliminary feasibility studies of frameless stereotactic liver surgery," *Arch. Surg.*, vol. 134, no. 6, pp. 644–650, Jun. 1999.

[15] J. M. Balter, L. A. Dawson, S. Kazanjian, C. McGinn, K. K. Brock, T. Lawrence, and R. T. Haken, "Determination of ventilatory liver movement via radiographic evaluation of diaphragm position," *Int. J. Radiation Oncol. Biol. Phys.*, vol. 51, no. 1, pp. 267–270, Sep. 2001.

[16] M. Clifford, F. Banovac, E. Levy, and K. Cleary, "Assessment of hepatic motion secondary to respiration for computer assisted interventions," *Comput. Aid. Surg.*, vol. 7, no. 5, pp. 291–299, 2002.

[17] J. W. Wong, M. B. Sharpe, D. A. Jaffray, V. R. Kini, J. M. Robertson, J. S. Stromberg, and A. A. Martinez, "The use of active breathing control (abc) to reduce margin for breathing motion," *Int. J. Radiation Oncol. Biol. Phys.*, vol. 44, no. 4, pp. 911–919, Jul. 1999.

[18] S. Nicolau, X. Pennec, L. Soler, and N. Ayache, "A complete augmented reality guidance system for liver punctures: First clinical evaluation," in *Proceedings of the International Conference on Medical Image Computing and Computer Assisted Intervention (MICCAI)*, ser. Lecture Notes Comput. Sci., J. Duncan and G. Gerig, Eds. New York: Springer-Verlag, 2005, vol. 3749, pp. 539–547.

[19] S. Nicolau, L. Goffin, and L. Soler, "A low cost and accurate guidance system for laparoscopic surgery: Validation on an abdominal phantom," in *ACM Symp. Virtual Reality Software Technol.*, Nov. 2005, pp. 124–133.

[20] F. Mourgues, T. Vieville, V. Falk, and È. Coste-Manière, "Interactive guidance by image overlay in robot assisted coronary artery bypass," in *Proceedings of the International Conference on Medical Image Computing and Computer Assisted Intervention (MICCAI)*, ser. Lecture Notes Comput. Sci., R. E. Ellis and T. M. Peters, Eds. New York: Springer-Verlag, 2003, pp. 173–181.

[21] G. Fichtinger, A. Deguet, K. Masamune, E. Balogh, G. S. Fischer, H. Mathieu, R. H. Taylor, S. J. Zinreich, and L. M. Fayad, "Image overlay guidance for needle insertion in CT scanner," *IEEE Trans. Biomed. Eng.*, vol. 52, no. 8, pp. 1415–1424, Aug. 2005.

[22] J. Ellsmere, J. Stoll, D. W. Rattner, D. Brooks, R. Kane, W. M. Wells, III, R. Kikinis, and K. Vosburgh, "A navigation system for augmenting laparoscopic ultrasound," in *Proceedings of the International Conference on Medical Image Computing and Computer Assisted Intervention (MICCAI)*, ser. Lecture Notes Comput. Sci., R. E. Ellis and T. M. Peters, Eds. New York: Springer-Verlag, 2003, pp. 184–191.

[23] J. Ellsmere, J. Stoll, W. Wells, R. Kikinis, K. Vosburgh, R. Kane, D. Brooks, and D. Rattner, "A new visualization technique for laparoscopic ultrasonography," *Surgery*, vol. 136, no. 1, pp. 84–92, Jul. 2004.

[24] J. Leven, D. Burschka, R. Kumar, G. Zhang, S. Blumenkranz, X. D. Dai, M. Awad, G. D. Hager, M. Marohn, M. Choti, C. Hasser, and R. H. Taylor, "Davinci canvas: A telerobotic surgical system with integrated, robot-assisted, laparoscopic ultrasound capability," in *Proceedings of the International Conference on Medical Image Computing and Computer Assisted Intervention (MICCAI)*, ser. Lecture Notes Comput. Sci.. New York: Springer- Verlag, 2005, vol. 3749, pp. 811–818.

[25] J. H. Siewerdsen, D. J. Moseley, S. Burch, S. K. Bisland, A. Bogaards, B. C. Wilson, and D. A. Jaffray, "Volume CT with a flat-panel detector on a mobile, isocentric c-arm: Pre-clinical investigation in guidance of minimally invasive surgery," *Med. Phys.*, vol. 32, no. 1, pp. 241–254, Jan. 2005.

[26] Z. Yaniv and K. Cleary, Image-guided procedures: A review Computer Aided Interventions and Medical Robotics, Imaging Science and Information Systems Center, Department of Radiology, Georgetown University Medical Center, Washington, DC, Tech. Rep., Apr. 2006.

[27] M. Feuerstein, T. Mussack, S. M. Heining, and N. Navab, "Registrationfree laparoscope augmentation for intra-operative liver resection planning," in *Medical Imaging 2007: Visualization and Image-Guided Procedures*, ser. Proc. SPIE, K. R. Cleary and M. I. Miga, Eds. Bellingham , WA: SPIE, 2007.

[28] S. Kriminski, M. Mitschke, S. Sorensen, N. M. Wink, P. E. Chow, S. Tenn, and T. D. Solberg, "Respiratory correlated cone-beam computed tomography on an isocentric c-arm," *Phys. Med. Biol.*, vol. 50, no. 22, pp. 5263–5280, Nov. 2005.

[29] N. Navab, M. Feuerstein, and C. Bichlmeier, "Laparoscopic virtual mirror—New interaction paradigm for monitor based augmented reality," *Virtual Reality*, pp. 43–50, Mar. 2007.

[30] M. Tuceryan, D. S. Greer, R. T. Whitaker, D. E. Breen, C. Crampton, E. Rose, and K. H. Ahlers, "Calibration requirements and procedures for a monitor-based augmented reality system," *IEEE Trans. Visual. Comput. Graphics*, vol. 1, no. 3, pp. 255–273, Sep. 1995.

[31] J. D. Stefansic, A. J. Herline, Y. Shyr, W. C. Chapman, J. M. Fitzpatrick, and R. L. Galloway, "Registration of physical space to laparoscopic image space for use in minimally invasive hepatic surgery," *IEEE Trans. Med. Imag.*, vol. 19, no. 10, pp. 1012–1023, Oct. 2000.

[32] R. Shahidi, M. R. Bax, C. R. Maurer, Jr., J. A. Johnson, E. P. Wilkinson, B. Wang, J. B. West, M. J. Citardi, K. H. Manwaring, and R. Khadem, "Implementation, calibration and accuracy testing of an image-enhanced endoscopy system," *IEEE Trans. Med. Imag.*, vol. 21, no. 12, pp. 1524–1535, Dec. 2002.

[33] F. Vogt, S. Krüger, H. Niemann, and C. Schick, "A system for real-time endoscopic image enhancement," in *Proceedings of the International Conference on Medical Image Computing and Computer Assisted Intervention (MICCAI)*, ser. Lecture Notes Comput. Sci., R. E. Ellis and T. M. Peters, Eds. New York: Springer-Verlag, 2003, pp. 356–363.

[34] J. Heikkilä and O. Silvén, "A four-step camera calibration procedure with implicit image correction," in *Proc. IEEE Conf. Comput. Vision Pattern Recognit. (CVPR)*, Jun. 1997, pp. 1106–1112.

[35] Z. Zhang, "A flexible new technique for camera calibration," *IEEE Trans. Pattern Anal. Mach. Intell.*, vol. 22, no. 11, pp. 1330–1334, Nov. 2000.

[36] R. Tsai and R. Lenz, "Real time versatile robotics hand/eye calibration using 3-D machine vision," in *Proc. IEEE Int. Conf. Robot. Automat.*, 1988, vol. 1, pp. 554–561.

[37] K. Daniilidis, "Hand-eye calibration using dual quaternions," *Int. J. Robot. Res.*, vol. 18, pp. 286–298, 1999.

[38] M. Mitschke and N. Navab, "Recovering projection geometry: How a cheap camera can outperform an expensive stereo system," in *Proc. IEEE Conf. Comput. Vision Pattern Recognit. (CVPR)*, 2000, vol. 1, pp. 193–200.

[39] T. Yamaguchi, M. Nakamoto, Y. Sato, K. Konishi, M. Hashizume, N. Sugano, H. Yoshikawa, and S. Tamura, "Development of a camera model and calibration procedure for oblique-viewing endoscopes," *Comput. Aided Surg.*, vol. 9, no. 5, pp. 203–214, 2004.

[40] N. Navab, A. R. Bani-Hashemi, M. M. Mitschke, D. W. Holdsworth, R. Fahrig, A. J. Fox, and R. Graumann, "Dynamic geometrical calibration for 3-D cerebral angiography," in *Medical Imaging 1996: Physics of Medical Imaging*, ser. Proc. SPIE. New York: Springer-Verlag, 1996, vol. 2708, pp. 361–370.

[41] D. Ritter, M. Mitschke, and R. Graumann, "Markerless navigation with the intra-operative imaging modality siremobil iso $- c^{3D}$," *Electromedica*, vol. 70, no. 1, pp. 31–36, 2002.

[42] T. Sielhorst, M. Feuerstein, J. Traub, O. Kutter, and N. Navab, "Campar: A software framework guaranteeing quality for medical augmented reality," *Int. J.Comput. Assisted Radiol. Surg.*, vol. 1, pp. 29–30, Jun. 2006.

[43] M. Y. Wang, C. R. Maurer, Jr., J. M. Fitzpatrick, and R. J. Maciunas, "An automatic technique for finding and localizing externally attached markers in CT and MR volume images of the head," *IEEE Trans. Biomed. Eng.*, vol. 43, no. 6, pp. 627–637, Jun. 1996.

[44] S. Nicolau, A. Garcia, X. Pennec, L. Soler, and N. Ayache, "Augmented reality guided radio-frequency tumor ablation," *Comput. Animation Virtual World* vol. 16, no. 1, pp. 1–10, 2005.

[45] R. Hartley and A. Zisserman, *Multiple View Geometry in Computer Vision*, 2nd ed. Cambridge, U.K.: Cambridge Univ. Press, 2003.

[46] E. Trucco and A. Verri, *Introductory Techniques for 3-D Computer Vision*. Upper Saddle River, NJ: Prentice Hall, 1998.

[47] P. Sturm, S. Ramalingam, and S. K. Lodha, "On calibration, structure-from- motion and multi-view geometry for panoramic camera models," presented at the Panoramic Photogrammetry Workshop Berlin, Germany, 2005.

[48] S. Gold and A. Rangarajan, "A graduated assignment algorithm for graph matching," *IEEE Trans. Pattern Anal. Mach. Intell.*, vol. 18, no. 4, pp. 377–388, Apr. 1996.

[49] M. W. Walker, L. Shao, and R. A. Volz, "Estimating 3-d location parameters using dual number quaternions," *CVGIP: Image Underst.*, vol. 54, no. 3, pp. 358–367, 1991.

[50] S. Nicolau, X. Pennec, L. Soler, and N. Ayache, "An accuracy certified augmented reality system for therapy guidance," in *Proceedings of the 8th European Conference on Computer Vision (ECCV 04)*, ser. Lecture Notes Comput. Sci.. New York: Springer-Verlag, 2004, vol. 3023, pp. 79–91.

[51] E. Euler, S. Heining, C. Riquarts, and W. Mutschler, "C-arm-based threedimensional navigation: A preliminary feasibility study," *Comput. Aid. Surg.*, vol. 8, no. 1, pp. 35–41, 2003.

[52] P. A. Grützner, A. Hebecker, H. Waelti, B. Vock, L.-P. Nolte, and A. Wentzensen, "Clinical study for registration-free 3-D-navigation with the siremobil iso $-$ c^{3D} mobile c-arm," *Electromedica*, vol. 71, no. 1, pp. 7–16, 2003.

[53] J. West and C. Maurer, "Designing optically tracked instruments for image-guided surgery," *IEEE Trans. Med. Imag.*, vol. 23, no. 5, pp. 533–545, May 2004.

[54] G. S. Fischer and R. H. Taylor, "Electromagnetic tracker measurement error simulation and tool design," in *Proc. Int'l Conf. Medical Image Computing and Computer Assisted Intervention (MICCAI)*, ser. Lecture Notes Comput. Sci., J. S. Duncan and G. Gerig, Eds. New York: Springer-Verlag, 2005, vol. 3750, pp. 73–80.

[55] M. Bauer, M. Schlegel, D. Pustka, N. Navab, and G. Klinker, "Predicting and estimating the accuracy of vision-based optical tracking systems," in *Proc. IEEE ACM Int. Symp. Mixed Augmented Reality (ISMAR)*, Santa Barbara, CA, Oct. 2006, pp. 43–51.